Environmental radioactivity in a sediment core from Algiers Bay: Radioecological assessment, radiometric dating and pollution records

Djamel Taieb Errahmani[a,b], Abdelkader Noureddine [b], José María Abril-Hernández [c,*], Mostefa Boulahdid [b]

[a] Centre de Recherche Nucléaire d'Alger (CRNA), Commissariat à l'Energie Atomique. 02 Bd. Frantz Fanon, Box.399, Algiers, Algeria
[b] Laboratoire des Ecosystèmes Marins et littoraux, Ecole Nationale Supérieure des Sciences de la Mer et de l'Aménagement du Littoral (ENSSMAL), BP 19, Campus Universitaire de Dely Brahim, Bois des Cars, Alger, Algeria
[c] Departamento de Física Aplicada I, ETSIA, University of Seville, Spain

ABSTRACT

Keywords:
Algiers bay
Sediment core
Radiometric dating
^{210}Pb
^{137}Cs
Pollution records

The sedimentary system of the Algiers Bay has been impacted in the last decades by the exponential increases in population, urbanism and industrial activities of the city of Algiers, and by episodic floods, mudflows, earth-quakes and tsunamis. Activity concentrations of environmental gamma-emitters, namely ^{210}Pb, ^{226}Ra, ^{40}K, ^{228}Ra, ^{228}Th and ^{137}Cs, were measured in a sediment core sampled in 2015 at the central zone of this bay, at 73 m depth from the surface water. The ^{210}Pb-based radiometric dating was challenging due to the incomplete recovery of the inventory, the absence of ^{137}Cs peaks, and the failure of classical models. The analysis of clusters in the logarithmic plot of the excess ^{210}Pb versus mass depth profile allowed for establishing a reliable chronology. Fluxes of excess ^{210}Pb and sediment accumulation rates (SAR) have both varied over the last five decades. Recent SAR values are of 0.73 ± 0.21 g cm^{-2}y^{-1}. Major and trace elements were determined by X-Ray Fluorescence in some selected sediment slices. Moderate enrichments have been observed for Mn, Zn, Br, Rb, Sr, Y and Pb in the 0–1 cm sediment layer (when using Al as normalization element), being governed by Fe-rich carriers. The major impact is observed in the carbon content, which increased by two orders of magnitude (from their basal values) for three decades since early 70's.

The dataset also allowed for a radioecological assessment in the area, performed using the ERICA software.

1. Introduction

The study in sediment cores of the ^{210}Pb found in excess with respect to its parent radionuclide ^{226}Ra (labelled ^{210}Pb$_{exc}$ hereafter) has shown to provide useful insights on the functioning of the sedimentary systems at a centennial time scale (Robbins, 1978; Carroll and Lerche, 2003; Mabit et al., 2014). Independent chronostratigraphic information can be provided by ^{137}Cs, a man-made radionuclide first introduced in the environment after the atmospheric nuclear weapon tests (Robbins and Edgington, 1975; Sánchez et al., 1992; Abril, 2004).

A summary of the most known ^{210}Pb-based dating models can be found in Mabit et al. (2014). The most widely used models are CRS (assuming a constant ^{10}Pb$_{exc}$ flux), CIC (assuming a constant ^{10}Pb$_{exc}$ initial activity concentration) and the CF-CS (assuming constant flux and constant sedimentation rate). A detailed presentation of these models can be seen, among others, in Sánchez-Cabeza and Ruíz-Fernández

(2012). In anthropogenic-impacted and/or high energy systems the ^{210}Pb flux onto the sediments may show non-random temporal variability, leading to the failure of classical dating models (Abril, 2019).

Studies on environmental radioactivity in the Algerian marine coastal zone are scarce. They include the distribution of anthropogenic radionuclides in the water column (Lee et al., 2006, Noureddine et al., 2008), ^{137}Cs in seawater, surficial sediments and sediment cores (Noureddine et al., 2006). The ^{210}Pb-based radiometric dating of recent sediments was applied to some sediment cores (Noureddine et al., 2008). The nearest one to the Algiers Bay was collected at a depth of 1220 m from the surface water.

During the last decades, the city of Algiers has experienced an intense increase in population, urbanization and industrialization, noticeably affecting the flows of matter and pollutants to its bay. An important harbour is integrated in the Algiers Bay. It has been continuously expanded, with major works carried out from the beginning of the 50's

until late 80's. Historically, Algiers was mainly supplied with water from Mitidja and Sahel Dunes aquifers, and with surface waters from the *Côtier Algérois* basin. In the mid-nineties water shortages were a prevailing phenomenon, so since 2002, new dams, surface water transfer systems, and desalination plants have been built (Naimi-Ait-Aoudia and Berezowska-Azzag, 2014). Two major oueds flow to the Algiers Bay, namely Oued El-Harrach (regulated by a dam) and that of El-Hamiz, fed by waste waters of the city and the waters of the plains of the Metidja.

Benamar et al. (1999) have reported high concentrations of copper and lead in surficial sediments from the central and western sectors of the bay, near the main emission of waste waters and of Algiers harbour. For their part, Boulahdid et al. (2013) found anomalous concentrations of zinc, copper and chromium at 6 cm depth in the sediments of a core taken at a depth of 30 m in the vicinity of the mouth of El Harrach River. In 1999, as part of the activities of the Mediterranean Action Plan (MAP) and the Mediterranean Pollution program (MEDPOL), the bay of Algiers was identified by UNEP/WHO as one of the hotspots priority pollution among 8 in Algeria and 131 in the Mediterranean Sea (UNEP/WHO, 1999).

In addition to the anthropogenic pressure, the Algiers Bay has been impacted by a diversity of natural hazards. The most important historical floods recorded in the area are those of 1954, 1960, 1974 and 2007 (Aroua and Berezowska-Azzag, 2009). On 10 November 2001, northern Algeria was hit by a heavy rainstorm and the Bab El Oued district of Algiers was devastated by cataclysmic floods and mudflows (Machane et al., 2008). The Bay of Algiers is located in a seismic zone with active faults triggering important earthquakes and sometimes small tsunamis. The latest important earthquakes took place in 1980 (at El Asnamin, Ms 7.3) and 2003. This last, with Ms 6.8, and with epicentre located a few km offshore, triggered a tsunami which was recorded in a large number of stations in the central and western Mediterranean Sea (Vecchio et al., 2014). On August 2014, a moderate-sized earthquake struck the city of Algiers, likely triggered by and active fault in the same bay of Algiers, according to Benfedda et al. (2017). Additionally, along the dunar cordon of the Algiers Bay, the combination of natural erosion and the intensive sand extraction produce the backward displacement of the coastal string (Chemrouk and Chabbi, 2016).

The aim of this paper is getting some insights on the sedimentary conditions and the recent pollution history in the Algiers Bay through the measurement of natural and artificial radionuclides, namely ^{210}Pb, ^{226}Ra, ^{228}Ra, ^{228}Th, ^{40}K and ^{137}Cs, along with major and trace elements, in a sediment core sampled at 73 m depth from the surface water. It has the value of reporting temporal trends of pollution in this coastal area, affected by anthropogenic and natural stresses, and scarcely studied. The ^{210}Pb-based radiometric dating is challenging since the high sediment accumulation rate (SAR) prevented the total recovery of the ^{210}Pb$_{exc}$ profile (and inventory) with our coring device, and it lacked of a clear trend-line in the deepest layers to support the reference-SAR method. The ^{137}Cs profile did not show distinct peaks for establishing independent reference dates. Under the dynamic sedimentary conditions above described the classical dating models failed, since their assumptions of constant values over time for fluxes (CRS model), initial activity concentrations (CIC model) or both (CF-CS model) did not hold. The holistic analysis of the whole dataset along with updated modelling approaches, including the analysis of clusters in the ^{210}Pb$_{exc}$ vs. mass depth profile (Abril, 2019) have shown to be useful for deriving a reliable chronology. Thus, the methodological procedures may be also of interest for the international scientific community dealing with environmental studies requiring the radiometric dating of recent sediments. The measured activity concentrations for the studied radionuclides also allowed for the first radioecological assessment in the area, performed with the ERICA tool (Larsson, 2008).

2. Materials and methods

2.1. Sampling and sample treatment

The studied site in the Algiers Bay has been briefly described above. Concerning climate, Algiers has a Mediterranean climate with hot and dry summers, while winters are cool and wet. The average temperature is 17.7 °C and the average annual rainfall is 707 mm, although it is very irregular and unevenly distributed in space.

A cylindrical sediment core of 45 cm length and 8.5 cm diameter was collected in September 2015 in the Algiers Bay at geographical coordinates 36°47.997′ N, 3°7.793′ E. The water depth was 73 m from the surface water. The sampling site is shown in Fig. 1. An Uwitec corer was used for sampling. It was operated from the *Grine Belkacem* research vessel, belonging to the Centre National de Recherche et de Développement de la Pêche et de L'Aquaculture (CNRDPA). The sediment core was frozen on board at a temperature of −18 °C, and sectioned at the laboratory into sections of 1–2 cm thick using a core slicer. Samples were put into plastic containers till oven drying at 70 °C to constant weight. They were grounded to fine powder using centrifugal grinder Retsch S100, and homogenized before analysis.

The water content in each sediment slice was calculated from the wet and dry weights, while bulk densities were determined by the ratio between the dry weight and the known volume for each slice.

Prior to gamma analysis, the sediment samples were sealed in Petri dishes to avoid ^{222}Rn escape, and stored for a period of at least three weeks to ensure secular equilibrium among ^{226}Ra and its progeny radionuclides ^{214}Bi and ^{214}Pb.

Loss on ignition (LOI) analysis were used as a proxy for estimating the organic matter content of selected sediment core samples. Two grams of dry sample were ignited at 480 °C for 4 h (Luczak et al., 1997).

2.2. Gamma spectrometry analysis

Gamma spectrometry measurements were performed to determine ^{210}Pb, ^{212}Pb, ^{214}Pb, ^{228}Ac, ^{40}K and ^{137}Cs activity concentrations using a coaxial High purity Germanium (HPGe) detector with a 40% of relative efficiency (a GX4018 from Canberra), and Genie-2000 software. Activity concentrations of ^{226}Ra were estimated through its progeny radionuclide ^{214}Pb. For radionuclides from the ^{232}Th series, ^{228}Ra was estimated through ^{228}Ac, and ^{228}Th through ^{212}Pb. Unsupported ^{210}Pb was determined for each slice by subtracting ^{226}Ra from the total ^{210}Pb activity concentration. The energies considered for the activity calculations were: 46.5 KeV for ^{210}Pb, 238.6 KeV for ^{212}Pb, 295.2 and 351.9 KeV for ^{214}Pb, 661.6 KeV for ^{137}Cs, 911.2 KeV for ^{228}Ac and 1460.8 KeV for ^{40}K. Counting times ranged between 20.3 and 48 h.

Energy and resolution calibrations were determined using point-sources of ^{241}Am, ^{137}Cs and ^{60}Co. The detector efficiency was calibrated using in–house calibration sources prepared by spiking separately a local marine sediment from the bay with liquid radioactive sources of ^{152}Eu and ^{133}Ba. Due to the mass variations of core samples, four standards for each tracer at different masses (25, 50, 75 and 100 g) were prepared with the same geometry as the samples. EFFTRAN software (Vidmar, 2005) was used for true coincidence summing corrections. This allowed for fitting the efficiency as a continuous function of the energy, and this for each mass. Thus, for any given photo-peak (e.g., the 46.5 keV emission for ^{210}Pb) there were four values for the efficiency as a function of the mass, which in all the cases followed a well-defined linear trend (e.g., r = - 0.998, p = 0.0021 for ^{210}Pb). For samples with intermediate masses, interpolations in the efficiency vs mass curve for each gamma emission were performed. The analytical procedure was checked using the proficiency test soil sample IAEA TEL 2018 (natural soil spiked with anthropogenic gamma emitter radionuclides). Two samples of the IAEA soil, of 50 g and 100 g, were prepared and measured as the samples from the studied sediment core. Table S-1, in electronic supplementary material, reports the measured activity concentrations
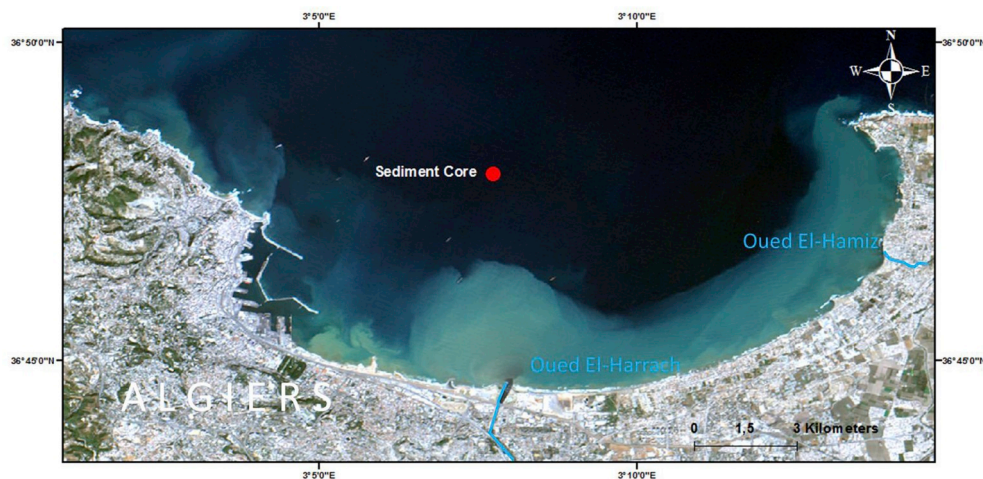
2

Fig. 1. The Algiers Bay with indication of the sampling site for the studied core. Satellite image from USGS/NASA Landsat, October 2nd' 2015. It shows clouds of suspended particulate matter.

for ^{210}Pb, ^{214}Pb and ^{137}Cs, compared against the target values.

2.3. Chemical and mineralogical compositions

Major and trace elements in sediment samples from selected depths in the core were analyzed by Wavelength –Dispersive X-Ray Fluorescence Spectrometer (WDXRF), using a Panalytical Philips Magix Pro and PW2440 model. Two grams of each sediment sample were prepared as pressed pellets using a licowax binder at a pressure of 18 tons, and then measured for 24.5 min time.

The mineralogical composition of sediment samples was determined by powder X-Ray diffractometry, using a PANalytical X'pert pro diffractometer equipped with a Cu-Kα radiation (1.54 Å) operated at 45 KV and 40 mA. Scans were performed in 2θ range from 5.01 to 84.99°, with a step of 0.02° and 1.8 s for each step. Phases were identified using Philips Highscore software.

2.4. Radioecological risk assessment

Because of the lack of previous studies, present results will be used for a radio-ecological assessment conducted with the ERICA tool. The mean activity concentrations found in the 0–10 cm of the core for ^{137}Cs, ^{210}Pb, ^{226}Ra, ^{228}Ra and ^{228}Th will support the application of the Tier 2 of version 1.2.1 of ERICA-tool to estimate activity concentrations and doses in eight selected biota (*benthic fish, crustaceans, macroalgae, mollusc-bivalve, pelagic fish, phytoplankton, polychaete worm* and *zooplankton*). We used the ERICA library for K_d values, (i.e., the ratio of activity concentration in sediment to that in water) and concentration ratios, CR (i.e., the ratio of activity concentration in the whole body of an organism to that in media) for the marine environment. The derived activity concentrations in the selected biota were then further processed by the ERICA-tool by selecting defined occupancy factor(s) of each biota and the dose conversion coefficients, DCCs (i.e., dose rate per unit activity concentration in the organism or media) – see Brown et al. (2016). Default settings were used, as in Klubi et al. (2017). The above estimated concentrations also served for calculating the dose to human due to the consumption of seafood products. The ingestion rate of each biota class, k, denoted as IR_k, was documented from local uses. The 50 year committed effective dose, E_{ing} (given in Sv), is then (UNSCEAR, 2008):

$$E_{ing} = \sum_{k,j} C_{k,j} e_{j,\ ing} IR_k \ , \tag{1}$$

where j refers to radionuclides and k to the type of food; $C_{k,j}$ is the activity concentration (Bq/kg) and $e_{j;ing}$ is the coefficient from conversion

from intake to committed effective dose integrated for 50 years for adults (UNSCEAR, 2008).

3. Results and discussion

3.1. The experimental dataset

Table 1 reports results for the water content, LOI percentage, dry mass thickness and the activity concentrations for the target radionuclides in the sediment core from Algiers Bay. The elemental composition determined by WD-XRF is reported in Table 2 for samples from five selected depth intervals within the core. The mineralogical composition (determined by X-R diffractometry) is reported in Table 3 for the same depth intervals.

Activity concentrations in the top sediment slices are of the same order than those reported by Benamar et al., (1999) for surficial sediments sampled within the bay.

The ^{228}Ra/^{226}Ra isotopic ratio was found to be 1.39 ± 0.14 (mean and standard deviation, all the sediment slices). Benamar et al., 1999 reported values ranging from 0.6 to 2.2 for this ratio, being of 1.6 around the sampling site of the core studied in this work. It is also similar to the mean value of 1.6 reported by Klubi et al. (2017) for sediment cores sampled in the Pra and Volta estuaries, in Ghana. The ^{228}Th/^{228}Ra isotopic ratio was 0.98 ± 0.18 (mean and standard deviation), being close to the radioactive secular equilibrium.

The mineralogical composition of crystalline phases (Table 3) remains quite uniform downcore, and dominated by Illite, Quartz, Muscovite and calcium-carbonates. The elemental composition (Table 2) reveals noticeable changes with depth in the concentration of C and some metals, such as Cu, Zn and Pb, which will be discussed after the radiometric dating of the sediment core.

3.2. Radioecological risk assessment

Table 4 reports the activity concentrations in reference organisms and the total dose rate per organism after applying ERICA with its default values for model parameters. The total dose rates to all the reference organisms fell below the screening value of 400 mGy·h^{-1}, and therefore being unlikely to cause harmful effects (UNSCEAR, 2008).

The representative seafood product from the Algiers Bay are benthic fish (*Mullus barbatus*), pelagic fish (*Sardina pilchardus*; *Sardinella aurita*) and crustacean (*Aristeus antennatus*), with relatively low mean annual consumption rates of 0.5, 2.0 and 0.5 kg per person (data from the Ministry of Agriculture, Rural Development and Fisheries of Algeria; Dr.

Table 1
Sediment characterization and activity concentrations[1] of the target radionuclides in the sediment core from Algiers Bay.

Depth (cm)	Water (%)	LOI (%)	Δm (g·cm^{-2})	^{210}Pb Bq/kg	^{226}Ra	^{137}Cs	^{228}Ra	^{212}Pb	^{4}K
0–1	45.4	15.0	0.576	133 ± 9	21.8 ± 0.8	3.8 ± 0.4	26 ± 10	36.4 ± 1.1	479 ± 15
1–2	47.4	7.5	0.701	136 ± 6	20.0 ± 0.7	3.5 ± 0.3	25 ± 4	26.0 ± 0.8	441 ± 27
2–3	45.9	7.2	0.628	149 ± 7	21.5 ± 0.7	3.4 ± 0.3	27 ± 7	28.0 ± 0.9	481 ± 30
3–4	47.2		0.817	127 ± 7	21.3 ± 0.6	3.3 ± 0.3	26 ± 6	27.8 ± 0.8	461 ± 29
4–5	44.1	7.5	0.714	136 ± 6	20.3 ± 0.7	3.5 ± 0.2	26 ± 4	27.8 ± 0.8	447 ± 28
5–6	45.1	7.2	0.906	131 ± 5	19.6 ± 0.6	3.8 ± 0.3	26 ± 4	26.7 ± 0.7	466 ± 30
6–7	42.8	7.5	0.644	122 ± 5	18.7 ± 0.7	4.0 ± 0.3	26 ± 4	26.7 ± 0.8	462 ± 28
7–8	41.6	7.1	0.747	116 ± 5	20.6 ± 0.7	3.8 ± 0.2	27 ± 5	26.7 ± 0.8	466 ± 29
8–9	41.8	7.1	1.076	110 ± 5	20.0 ± 0.7	3.8 ± 0.2	24 ± 4	25.7 ± 0.8	462 ± 30
9–10	41.3	4.7	0.923	89 ± 4	21.0 ± 0.6	4.0 ± 0.3	29 ± 8	26.0 ± 0.7	474 ± 30
10–12	40.6	6.2	1.806	80 ± 8	20.1 ± 1.6	4.6 ± 0.4	30 ± 6	26.8 ± 2.0	471 ± 35
12–14	40.2		1.941	70 ± 8	21.1 ± 1.9	4.7 ± 0.5	30 ± 10	26.8 ± 2.4	490 ± 38
14–16	39.1		1.614	69 ± 6	20.9 ± 1.3	5.4 ± 0.4	31 ± 5	28.8 ± 1.7	500 ± 36
16–18	39.0		1.895	60 ± 7	22.7 ± 2.0	5.1 ± 0.5	32 ± 6	27.6 ± 2.3	504 ± 38
18–20	39.7		1.753	56 ± 6	21.8 ± 1.6	5.4 ± 0.5	31 ± 10	30.9 ± 2.2	468 ± 35
20–22	41.5		1.842	51 ± 6	21.2 ± 1.7	4.9 ± 0.4	32 ± 6	27.1 ± 2.2	480 ± 36
22–24	41.5		1.959	39 ± 5	20.0 ± 1.9	4.3 ± 0.4	28 ± 5	18.3 ± 1.7	430 ± 33
24–26	41.4		1.750	33 ± 3	21.0 ± 1.6	5.0 ± 0.4	22 ± 4	34.6 ± 2.5	493 ± 37
26–28	40.8		1.806	38 ± 4	22.3 ± 1.8	4.9 ± 0.4	30 ± 5	22.8 ± 1.7	510 ± 38
28–30	42.2		1.758	37 ± 4	21.6 ± 1.6	4.1 ± 0.4	33 ± 6	28.1 ± 2.0	506 ± 38
30–32	43.1	8.4	1.609	28 ± 3	21.5 ± 1.4	4.3 ± 0.3	32 ± 6	28.0 ± 1.7	531 ± 38
32–34	44.4		1.967	28 ± 4	18.1 ± 1.7	4.4 ± 0.5	24 ± 5	22.0 ± 2.0	432 ± 34
34–36	43.0		1.899	28 ± 4	18.7 ± 1.6	5.6 ± 0.6	28 ± 10	29.3 ± 2.5	443 ± 34
36–38	42.6		1.803	33 ± 4	20.1 ± 1.6	6.0 ± 0.5	33 ± 6	29.2 ± 2.2	526 ± 39
38–40	41.6		1.773	26 ± 4	22.2 ± 1.7	6.6 ± 0.6	33 ± 11	33.9 ± 2.5	500 ± 37
40–42	40.3		1.844	33 ± 4	21.9 ± 1.8	7.5 ± 0.7	35 ± 6	31.5 ± 2.5	531 ± 40
42–44	38.0	8.3	1.783	36 ± 4	22.1 ± 1.7	7.4 ± 0.7	34 ± 11	35.6 ± 2.6	506 ± 38

[1]Mean and 1σ counting uncertainties.
Δm is the dry mass thickness, estimated from the total dry mass of sediment in each slice and the core cross sectional area (56.72 cm^2).

Table 2
Elemental composition determined by WDXRF in the sediment core from Algiers Bay.

Analyte	Depth interval in the sediment core				
	(0–1 cm)	(9–10 cm)	(18–20 cm)	(28–30 cm)	(42–44 cm)
C (%)	2.27	14.07	8.54	0.03	0.18
Na (%)	0.45	0.48	0.63	0.44	0.45
Mg (%)	3.65	3.89	5.86	4.31	4.18
Al (%)	5.26	5.62	6.38	7.30	7.13
Si (%)	64.80	70.31	73.28	82.17	82.32
P (%)	0.11	0.13	0.14	0.14	0.13
S (%)	0.19	0.22	0.30	0.36	0.32
Cl (%)	0.56	0.65	0.53	0.45	0.53
K (%)	0.33	0.36	0.48	0.53	0.47
Ca (%)	2.36	2.70	2.59	2.45	2.40
Ti (%)	0.12	0.12	0.14	0.16	0.16
V (%)	17.35	0.01	N.M.	0.01	0.00
Cr (ppm)	N.M.	63.4	N.M.	41.6	55
Mn (ppm)	241.2	79.4	48.4	139.8	73.6
Fe (%)	2.495	1.435	1.119	1.642	1.691
Cu (ppm)	80.7	15.8	22.7	N.M.	N.M.
Zn (ppm)	57.5	28.9	7.5	24.1	21.5
Ga (ppm)	8.6	9.1	3.8	N.M.	N.M.
Br (ppm)	23.9	13.7	5.6	10.3	12.8
Rb (ppm)	27.7	13.9	5.9	12.4	14.3
Sr (ppm)	82.1	57.8	27.3	57.1	53.4
Y (ppm)	6.9	2.2	1.9	6.1	3.1
Pb (ppm)	19.5	12	N.M.	N.M.	10.5

N.M.: Non measured.

Table 3
Mineralogical composition determined by X-Ray diffractometry in the sediment core from Algiers Bay. Phases are reported in %.

Phase	Depth interval in the sediment core				
	(0–1 cm)	(9–10 cm)	(18–20 cm)	(28–30 cm)	(42–44 cm)
Illite	34	35.6	34.3	37	36
Quartz	23	22.8	24.2	21	24
Muscovite	19	17.8	17.2	20	17
Calcium carbonate	14	13.9	15.2	12	14
Al Mg Hydroxide Silicate	7	6.9	7.1	8	7
Potassium Iron (III) oxide	2	2	1	1	1
Anatase	1	1	1	1	1

Kacher, personal communication). The ERICA-derived activity concentrations in these biota classes (Table 4) for the set of studied radionuclides served to estimate (by Eq. (1)) the committed effective dose integrated for 50 years for adults by using the conversion coefficients recommended by UNSCEAR (2008) for natural radionuclides, and ICRP (2012) for ^{137}Cs. It resulted of 3.2·10^{-5}Sv, which is far from producing any harmful effects (UNSCEAR, 2008).

3.3. Sediment dating by ^{210}Pb-based classical models

Fig. 2 plots the activity concentrations for ^{210}Pb$_{exc}$ and ^{137}Cs versus the mass depth, m, in the sediment core.

The CF-CS model assumes constant ^{210}Pb$_{exc}$ flux onto the sediment-water interface (SWI), and a constant sediment accumulation rate (SAR), w [ML^{-2}T^{-1}], which results in an exponential decrease of the activity concentration, $A(m)$, with m:

$$A(m) = A_0 e^{-\lambda m/w}, \tag{2}$$

where λ is the radioactive decay constant for ^{210}Pb. The best fit is shown in Fig. 2, first panel. The scaling factor is $\lambda/w = 0.084 \pm 0.006$ cm^{2}g^{-1}, which leads to a sedimentation rate of $w = 0.371 \pm 0.025$ g cm^{-2}y^{-1}. The Pearson's correlation coefficient is $r = -0.948$, but it is worth noting that high r values are a necessary, but not a sufficient condition for the reliability of the CF-CS model assumptions. The corresponding chronology (ages, $t = m/w$) is plotted in Fig. 2, second panel. The CF-CS age of the central point of the last measured slice is 102 ± 7 y (a date of 1914

Table 4

Radionuclide activity concentrations in sediment[1] and ERICA derived radionuclide activity concentrations and total dose rates in reference organisms.

Radionuclide	(Bq·kg^{-1})	Reference organisms (Bq·kg^{-1} fresh weight)							
		benthic fish	crustaceans	Macro-algae	mollusc-bivalve	pelagic fish	phytoplankton	polychaete worm	zooplankton
^{137}Cs	3.7	0.029	0.018	0.033	0.017	0.029	0.003	0.062	0.045
^{210}Pb	124.9	15.475	9.848	0.469	2.954	15.475	225.095	18.758	7.972
^{226}Ra	20.5	0.537	0.329	0.344	0.249	0.537	4.102	0.537	0.310
^{228}Ra	26.3	0.690	0.424	0.443	0.320	0.690	5.633	0.690	0.399
^{228}Th	27.8	0.005	0.133	0.016	0.006	0.005	2.552	0.006	0.025
Total Dose Rate	(µGy.h^{-1})	0.089	0.087	0.067	0.051	0.072	1.061	0.111	0.046

[1]Radionuclide activities in sediments correspond to the 0–10 cm depth interval, and they are reported in a dry weight basis.
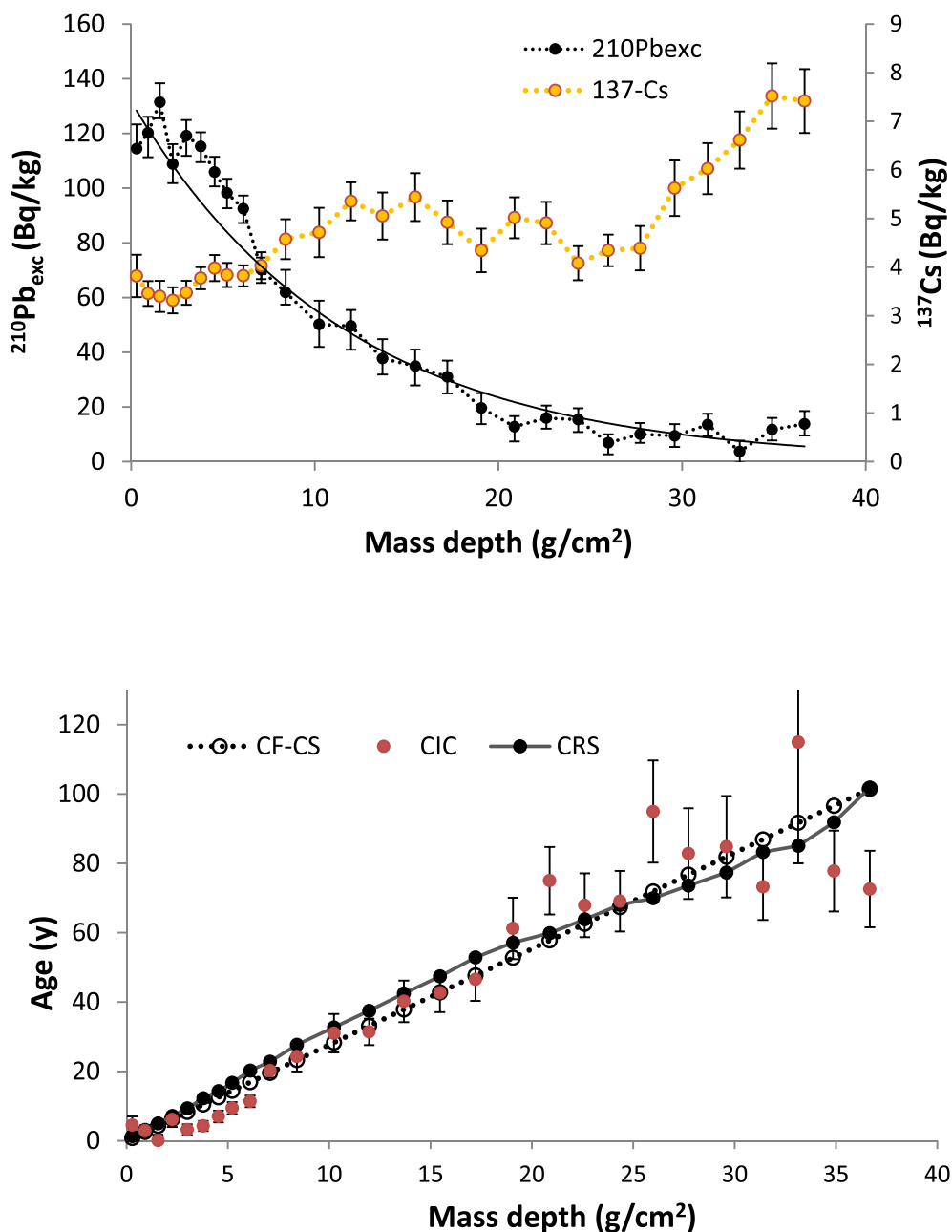
Fig. 2. ^{210}Pb$_{exc}$ and ^{137}Cs activity concentrations versus mass depth in the studied sediment core (first panel). The continuous line is the exponential fit from the CF-CS model (Eq. (2)). The second panel shows the chronologies obtained from the CF-CS, CIC and CRS models (see text for details). For the sake of simplicity error-bars are only depicted for CIC ages.

± 7). This is in contradiction with the ^{137}Cs profile, which shows an absolute maximum at the deepest layers, and so, they cannot be older than the first significant appearance of ^{137}Cs in the environment (middle 50's).

The CIC model assumes constant initial activity concentration, A_0, so the age of the sediment slice centered at mass depth m can be derived from the measured $A(m)$ value:

$$t = \frac{1}{\lambda} LN\left(\frac{A_0}{A(m)}\right). \tag{3}$$

The choice of A_0 is problematic, and here we selected the value of 128 Bq/kg with the criteria that the linear trend line of the CIC ages intercepts the origin at $m = 0$. The corresponding CIC chronology is shown in Fig. 2 (second panel). The age of the deepest layer is 72 ± 11 y (date 1944 ± 11), which is also inconsistent with the ^{137}Cs profile. It is worth noting that when A_0 shows random variability around a mean value, the CIC ages show random dispersion around a trend-line, which is the one with physical meaning.

The CRS model assumes a constant flux ^{210}Pb$_{exc}$ onto the SWI, which is maintained for long enough as to achieve a steady-state for the total inventory of ^{210}Pb$_{exc}$. The age of a sediment slice which ends at mass depth m is

$$t = \frac{1}{\lambda} LN\left(\frac{\Sigma_0}{\Sigma_m}\right), \tag{4}$$

where $\Sigma_m = \int_m^\infty A(m')dm'$ is the ^{210}Pb$_{exc}$ inventory laying below mass depth m; and Σ_0 is the total inventory below the SWI ($m = 0$). As seen in Fig. 2 the core length, m_L, is not long enough as to reach the equilibrium depth (^{210}Pb$_{exc}$ concentrations remains null below such a depth). Consequently the recovered inventory ($\int_0^{m_L} A(m')dm' = 15.0 \pm 0.4$ kBq·m^{-2}) is lower than Σ_0, and it is necessary estimating the missing part of the inventory. The usual correction method by the reference SAR (Appleby, 1998) is problematic in this case since ^{210}Pb$_{exc}$ activity concentrations show a flattening at the deepest layers, limiting the use of extrapolations. But using the exponential trend holding for the whole core (Fig. 2, first panel), a summing correction of 0.64 kBq·m^{-2} can be estimated. The resulting chronology is plotted in Fig. 2, second panel. The age of the last measured slice results of 103 ± 8 y, also in contradiction with ^{137}Cs data. It is worth noting that the agreement between CF-CS and CRS chronologies is not a proof of their reliability for the studied core.

Implicitly the above three classical models assume ideal deposition (in the terms described by Abril and Gharbi, 2012) and no post-depositional redistribution. Diffusion of particle bound radiotracers within the sediment requires the physical reworking of solids, moving up and down with a null mass flow; and this needs a forcing agent. Thus, invoking diffusion for ^{137}Cs but not for ^{210}Pb does not seem to be physically consistent (Abril, 2003a). Non-ideal deposition depends on the physic-chemical form of the incoming fluxes and on the sediment structure; and it can work with different intensities for these two radionuclides. It produces long penetrating tails in the ^{137}Cs profile (which cannot be observed in this case because the short core length), and a flattening and/or a sub-surface maximum in the ^{210}Pb$_{exc}$ profile (Abril and Gharbi, 2012). Alternatively, a flattening in the ^{210}Pb$_{exc}$ profile could reflect a homogenite – a relatively thick sediment layer deposited in an episodic event. But this last uses to correlate with discontinuities in the depth profiles of bulk density and/or other radiotracers (Abril et al., 2018). These questions will be discussed further below, within the holistic analysis of all the available sources of evidences from the present dataset.

3.4. Bulk density and normalized depth-distributions of multi-tracers

Fig. 3 plots the bulk density versus true depth in the sediment core. Method A uses the total dry mass and the known volume of the sediment
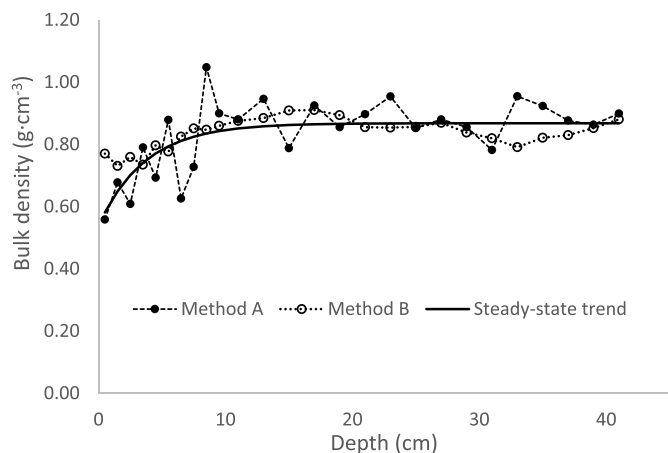

Fig. 3. Bulk density versus true depth in the sediment core. Method A uses the total dry mass and the known volume of the sediment slice; method B uses a two-phases sediment model with an uniform density for solids of 2.2 g cm^{-3}. Both estimates are corrected by the precipitated salts from the pore fluid (estimated from the water content and the salinity of seawater in the bay, 36.5 PSU). The continuous line plots the steady-state trend.

slice, as described in Section 2.1. The salinity of the pore fluid was not directly measured, but it is expected to be close to the mean salinity of seawater in the Algiers Bay, which is about 36.5 PSU (Noureddine et al., 2008). This, along with the measured water content (Table 1), allows correcting by the precipitated salts from the pore fluid (Dadey et al., 1992). Corrections are small, of 2.7% in average (range 2.2%–3.3%). It can be helpful comparing these estimates with the bulk density (ρ_b) arising from a two-phases model of the sediment, with uniform densities for solids (ρ_s) and pore water (ρ_w), and additive volumes (method B):

$$\rho_b = \frac{1 - f_w}{\frac{1 - f_w}{\rho_s} + \frac{f_w}{\rho_w}} \tag{5}$$

In Eq. (5) f_w is the fraction in weight of water. Results are plotted in Fig. 3, for $\rho_s = 2.2$ g cm^{-3} – a value lower than the commonly assumed of 2.5–2.6 g cm^{-3}, what highlights the contribution of organic matter and the remaining water films after drying at 70 °C. Method A is not limited by the assumptions involved in method B, but it is sensitive to slight uncertainties in the thickness of the layer when slicing. Thus, the discontinuity observed in the 7–9 cm interval does not appear with method B. The bulk density profile roughly follows the expected trend for a steady state compaction (Abril, 2003b, 2011), without clear evidences of discontinuities which could suggest homogenites or other drastic changes in the sedimentary conditions.

It is worth noting that corrections by precipitated salts are not necessary for the estimation of the CRS ages, since this model works with inventories (Eq. (4)), so the corrections in the mass thickness and in the activity concentrations mutually compensate. These corrections properly apply to the CRS-SARs and to the CF-CS and CIC models. In the studied core the corrections are small (about 2.7%) and thus, the chronologies (Section 3.3) remain essentially unchanged (e.g., an age of 101 ± 6 y is estimated for the deepest sediment slice, with the salt-corrected CF-CS model).

Fig. 4 plots the normalized (to their arithmetic means) activity concentrations of ^{226}Ra, ^{212}Pb (^{228}Th), ^{40}K and LOI vs. mass-depth in the studied sediment core. Normalization facilitates the comparison of the depth-distribution patterns for different analytes by using the same vertical and dimensionless scale. It is worth mention that ^{228}Ra has not been included since it is close to the secular equilibrium with ^{212}Pb, and thus, it does not add new information. ^{226}Ra and ^{40}K show quite uniform distributions with mass-depth. The same is true for ^{212}Pb but few excursions out of the main trend line (e.g., an anomalous high value at the top sediment slice). The LOI content of the uppermost sediment slice is
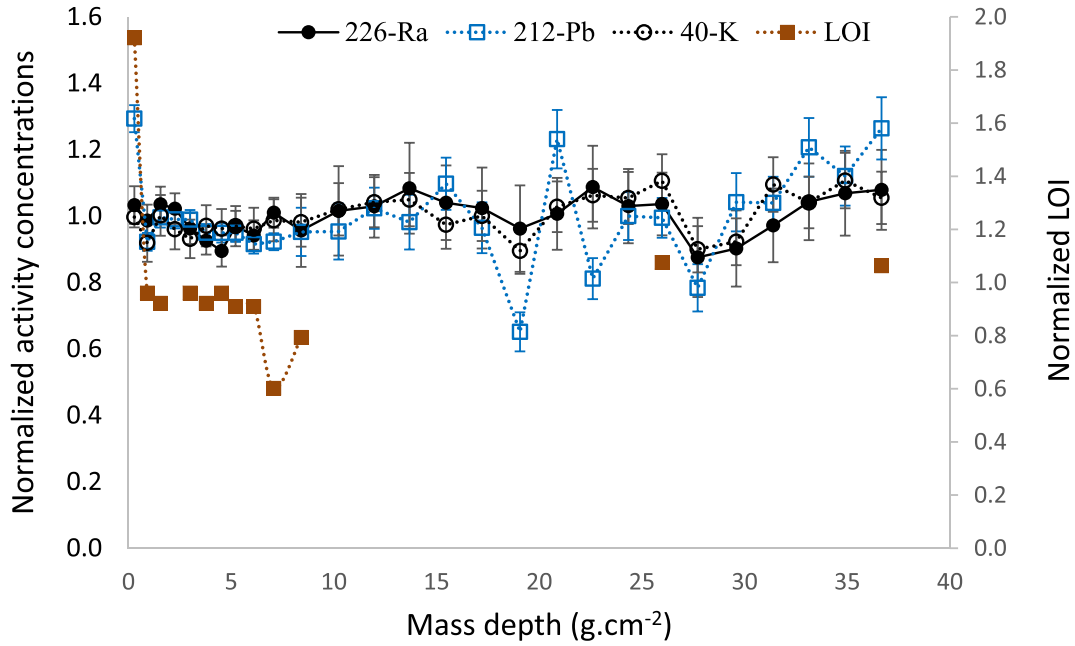
Fig. 4. Normalized (to their arithmetic means) activity concentrations of ^{226}Ra, ^{212}Pb (^{228}Th) and ^{40}K, and normalized LOI content versus mass depth in the sediment core from Algiers Bay.

also much higher than in the rest of the core. Overall, Fig. 4 does not reveal any noticeable disruptions in the sedimentary sequence.

On the light of present results, a homogenite can be discarded as the likely explanation of the plateau observed in ^{210}Pb$_{exc}$ in the deepest portion of the core, since it is not compatible with the structure of varying activity concentrations observed for ^{137}Cs in the same region (Fig. 2). Similarly, homogenite and physical mixing seem to be unlikely for explaining the flattening in the ^{210}Pb$_{exc}$ activity concentrations in the top sediment, because the fingerprint of active early compaction is preserved (Fig. 3), and because the singular high value of LOI in the first sediment slice.

3.5. $^{210}Pb_{exc}$ and ^{137}Cs inventories and fluxes onto the SWI

The incompletely recovered ^{210}Pb$_{exc}$ inventory was 15.0 ± 0.4 kBq·m^{-2}, what implies an equivalent constant ^{210}Pb$_{exc}$ flux onto the SWI ($F_{eq} = \lambda \Sigma_0$) greater than 465 ± 13 Bq·m^{-2} y^{-1}. This is much higher than the expected atmospheric deposition in the area, knowing that the worldwide atmospheric deposition is in the range 40–250 Bq·m^{-2}y^{-1} (Appleby, 1998). This discards pure water-column scavenging process, and suggests an important contribution of the ^{210}Pb$_{exc}$ already bound to the mass flows reaching the SWI. In these cases, ^{210}Pb$_{exc}$ fluxes are expected to be correlated with SAR (Abril and Brunskill, 2014).

Satellite images of the Algiers Bay often allow visualizing clouds of suspended particulate matter supplied by the oueds and by runoff and erosion along the shoreline (e.g., see Fig. 1). The transport can progress through deeper layers as the combined effect of horizontal advection and vertical settling. It is not unlikely that under some particular conditions these mass flows could reach the sampling site. The episodic floods and associated mudflows in the area, along with the anthropogenic impacts described in the Introduction section, may result in SAR and ^{210}Pb$_{exc}$ fluxes largely varying over time. Nevertheless, the application of the CRS model would be still possible in the case that such variability in ^{210}Pb$_{exc}$ fluxes was randomly distributed over time (Abril, 2019). This will be discussed further in Section 3.6.

The ^{137}Cs inventory measured in the 0–45 cm interval was 1920 ± 40 Bq·m^{-2}, but there is an unknown missing part of the total inventory due to the non-null ^{137}Cs concentrations below such 45 cm depth. It is known that ^{137}Cs fallout largely varied with geographical latitude and local

rainfall, and that in deep sea a large fraction of the integrated deposition remains for long in the water column (Noureddine et al., 2008). The integrated atmospheric deposition in European areas not affected by the Chernobyl accident were about 1400 Bq·m^{-2} (corrected by radioactive decay to the date of sampling in 2015; data for UK, after Wright, 2016). Consequently, it is also expected that the ^{137}Cs fluxes onto the SWI were contributed by both water column scavenging, and by the ^{137}Cs bound to the mass flows reaching the SWI.

Although there exist good records for historic ^{137}Cs atmospheric deposition, several pre-depositional and/or within-system processes may lead to different temporal patterns for the ^{137}Cs fluxes onto the SWI (Robbins et al., 2000). Here we explore some modelling approaches in an attempt to understand the main features of the measured ^{137}Cs vs mass depth profile. Let us consider a simple model consisting in a well-mixed water column of cross-sectional area S [L^2] and depth h [L], receiving the atmospheric deposition, F_{at} [Bq·L^{-2}T^{-1}], and transferring a flux F_S [Bq·L^{-2}T^{-1}] to the underlying sediment (physical dimensions in brackets). F_S can be written in terms of a mean settling-contributed SAR, w_S[M·L^{-2}T^{-1}], the k_d value for the studied radionuclide, and the concentration in the water column, C_w[Bq·L^{-3}]: $F_S = w_S \, S k_d C_w$. Thus, the following differential equation holds for $C_w(t)$:

$$\frac{dC_w}{dt} = \frac{F_{at}}{h} - \frac{w_S \, k_d}{h} C_w - \lambda C_w \qquad (6)$$

where λ [T^{-1}] is the radioactive decay constant for ^{137}Cs.

The activity concentration of ^{137}Cs in seawater at the site and time of sampling was measured, being of 1.00 ± 0.04 Bq·m^{-3} (data from authors' personal records). Using the activity concentration in the first sediment slice (Table 1), a local k_d value of 3.8·10^3 L/kg arises. Fig. 5 plots the solution of Eq. (6) using for F_{at} the historical records for UK (Wright, 2016), corrected by a normalization factor, Z, globally accounting the different geographical latitude and local rainfall, $h = 73$ m, and $w_S = 0.06$ g cm^{-2}y^{-1} (Model 1 in Fig. 5, with $Z \sim 1$). The value of w_S has been selected to better fit the available data (Fig. 5). Similar results can be obtained by a modified water-column model considering horizontal inputs (by exchanges with the surrounding water masses), as in Laissaoui et al. (2008), at a rate of 0.05 y^{-1}, and increasing the value of w_S to 0.15 g cm^{-2}y^{-1} (Model 2 in Fig. 5).

The above numerical exercises only have the value of a concept-

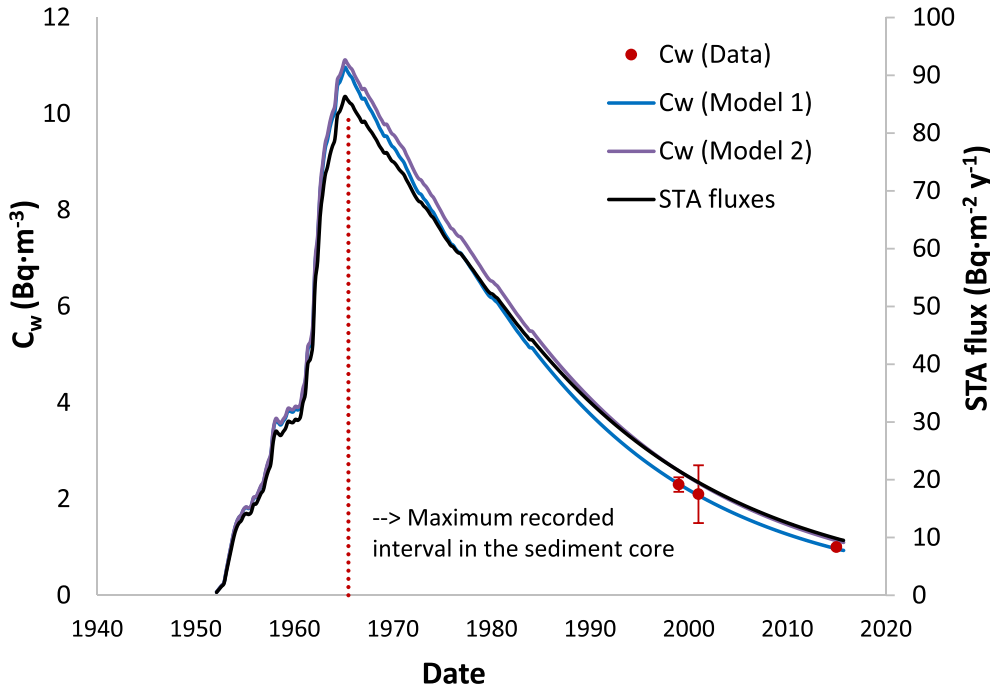**Fig. 5.** ^{137}Cs concentration in seawater (in Bq·m^{-3}) around the Algiers Bay (data for 1999 and 2001 are from Noureddine et al., 2008; while data for 2015 is from authors' personal records). Model 1 is the solution of Eq. (6) with local k_d value of $3.8 \cdot 10^3$ L/kg and atmospheric deposition from Wright (2016), with $h = 73$ m and $w_S = 0.06$ g cm^{-2}y^{-1}. Model 2 includes horizontal exchanges at a rate of 0.05 y^{-1}, with $w_S = 0.15$ g cm^{-2}y^{-1}. STA fluxes (in Bq·m^{-2}y^{-1}) are the solution of Eq. (7) with the same atmospheric deposition and $k_r = 0.026$ y^{-1}. The vertical dashed line delimits the maximum time-interval recorded in the sediment core (Fig. 2).

demonstration model, where SAR values account for the settling fluxes. These mass flows are much lower than the ones estimated from the classical models (Section 3.3), so the contribution of other mass flows (from continental runoff and shallower depositional areas) must be considered. Nevertheless, the integration of ^{137}Cs atmospheric fluxes in the catchment area has been widely described (McCall et al., 1984; Abril and García-León, 1994; Robbins et al., 2000). The simplest formulation can be found in Robbins et al. (2000), where it is designated as the system time averaging (STA) model. The fluxes onto the SWI, F_S, are expressed as a function of the atmospheric deposition, F_{at}, involving the radioactive decay constant of the radionuclide, λ, and a system's constant, k_r, with physical dimension of T^{-1}:

$$\frac{dF_S}{dt} = k_r F_{at} - (\lambda + k_r) F_S. \tag{7}$$

Fig. 5 plots the solution of Eq. (7) with F_{at} from Wright (2016) and $k_r = 0.026$ y^{-1} (this value has been selected to get a temporal pattern similar to that of Model 1 in Fig. 5).

As conclusion, it is expected an integration effect of the atmospheric ^{137}Cs fluxes in the water column and in the erosional areas contributing to the mass flows reaching the SWI at the core site. This integration effect would result in a ^{137}Cs profile in the sediment being a mirror-image of the curves depicted in Fig. 5, but to some extent distorted by varying sedimentary conditions. This is, the core is not long enough as capturing the peak, but only the declining trend line. Consequently the age of the deepest measured sediment-slice must be younger than the age of the ^{137}Cs peak in Fig. 5, which, due to the pre-depositional effects (Eqs. (6) and (7)), is slightly displaced to ~1965.

Direct contribution of ^{137}Cs fallout from Chernobyl is expected to be negligible in this area, but it affected the northern and eastern Mediterranean basins (Delfanti et al., 2003). Thus, the Levantine Intermediate Water (LIW) circulating through the Algerian Basin could carry some signal from Chernobyl, but their effects in the Algiers Bay are unlikely, since the Modified Atlantic Water (MAW) occupies the top 200 m layer of the Alboran Sea (Noureddine et al., 2008).

The above analyses suggest that ^{210}Pb$_{exc}$ and ^{137}Cs inputs on the SWI have been largely contributed by their activities bound to the mass flows from continental runoff and shallower depositional areas. Non-ideal deposition arises mainly from diffusion and the kinetic uptake of

dissolved radionuclides through the connected water pores and, to less extend, by depth distribution of colloidal and small grain size fractions (Abril and Gharbi, 2012), but it is quite unlikely for those radionuclides already bound to solid particles reaching the SWI. Consequently, the flattening observed in the ^{210}Pb$_{exc}$ profile in the top region of the core must obey to varying SAR and initial activity concentrations.

3.6. Analysis of clusters and piecewise models

Based upon a wide and systematic survey on varved sediments from marine, riverine and lacustrine environments, Abril and Brunskill, (2014) found that ^{210}Pb$_{exc}$ fluxes onto the SWI were highly variable in time and statistically correlated with SAR. As above discussed, this seems to be also the case for the studied core. This supports the application of the methodology of analysis of clusters developed by Abril (2019). Briefly, when persistent changes in environmental conditions shift the initial concentrations and/or the SARs towards different mean values, the plot Ln[$A(m)$] can show jump discontinuities and/or changes in the slope –$A(m)$ being the activity concentration of ^{210}Pb$_{exc}$.

Fig. 6, first panel, shows the Ln[$A(m)$] plot for the studied core, with two jump discontinuities and three transects. A linear fit has been applied to each transect, what allows estimating the mean sedimentary conditions (i.e., the mean values for SAR, initial activity concentrations and fluxes) – see Abril (2019). Results are summarized in Table 5. For transects 1 and 2 the linear fit is statistically significant at a confidence level higher than 95%, but it is poor for transect 3. Although with large propagated uncertainties, the mean values of initial activity concentrations have increased with time (from transect 3, in the deeper and older portion of the core, to transect 1, in its upper and younger portion). Mean SAR was high and with also high variability in the third transect (0.94 ± 0.69 g·cm^{-2}y^{-1}), smaller and quite uniform in the second (0.385 ± 0.027 g·cm^{-2}y^{-1}), and rising up to 0.74 ± 0.21 g·cm^{-2}y^{-1} in the first transect. As result, the mean values of fluxes have changed over time. Consequently, under these sedimentary conditions, the CRS model hardly can provide reliable results, even under its piecewise version – in the case that a reference date was known (Abril, 2019).

The piecewise versions of the CF-CS and CIC models have been applied to the studied core using, respectively, the SAR values and the initial activity concentrations reported in Table 5. The resulting
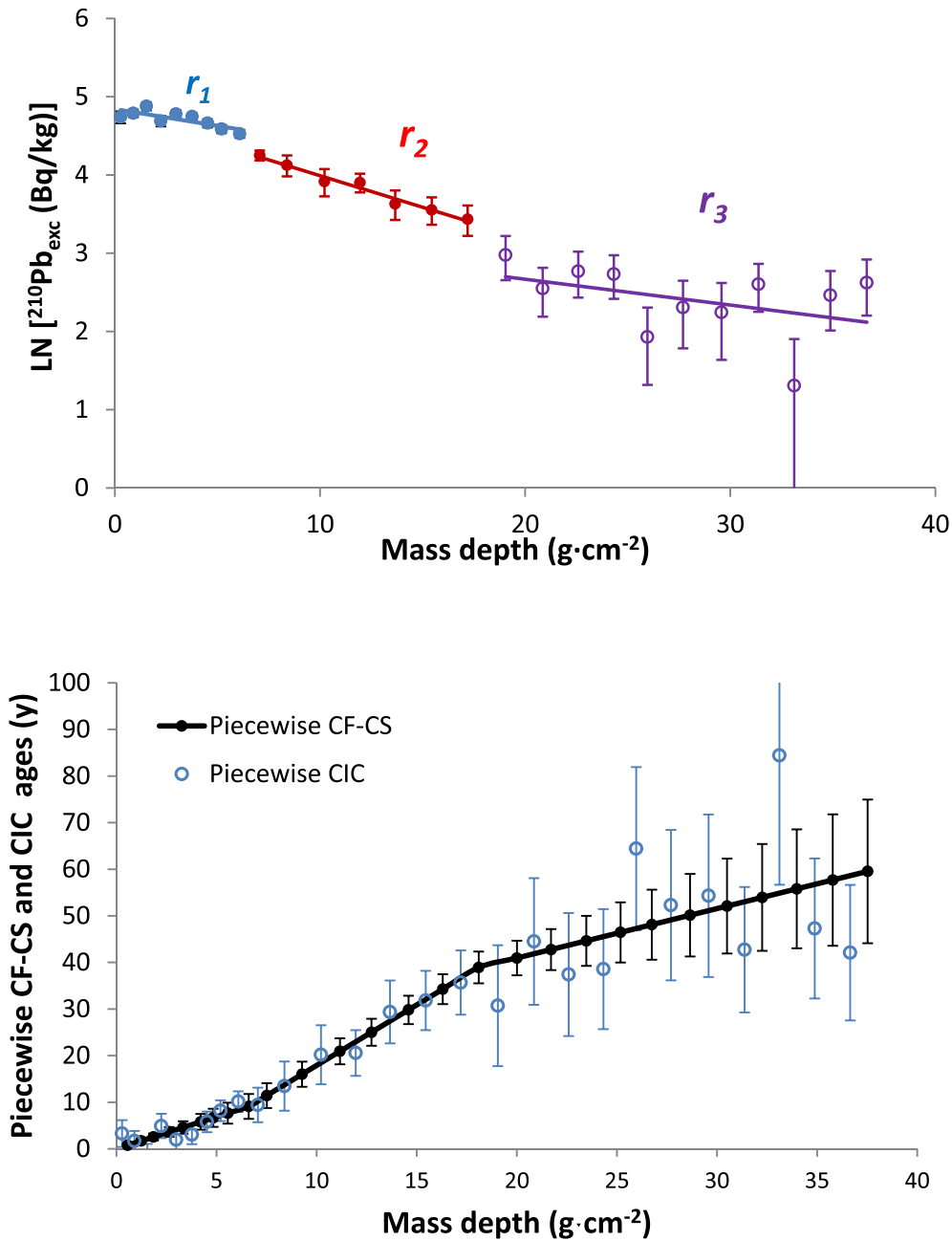
Fig. 6. Logarithmic plot of $^{210}Pb_{exc}$ activity concentrations in the sediment core from Algiers Bay, with the identification of three clusters defined by jump discontinuities and changes in the slope (first panel). The fitting parameters are reported in Table 5. The chronologies from piecewise CF-CS and CIC models are shown in the second panel.

chronologies, along with the propagated uncertainties, are depicted in Fig. 6, panel 2. This must be understood as providing a reasonable proxy to the true chronology, being particularly limited for the third transect. Again, for the CIC model the physically meaningful chronology is the trend line defined by the cloud of model ages. The piecewise CF-CS age for the central point of the last sediment slice is 59 ± 15 y, which is compatible with the age of <51 y expected from the ^{137}Cs profile and the analysis of Fig. 5.

The third transect is poorly described by both models. The CIC chronology shows two ages being too old and out of the trend-line. This suggests that true initial activity concentrations in these two layers should have been lower by a factor 2 than the mean value assumed for this transect (Table 5). They are likely linked to large depositional events. Thus, sedimentary conditions in this transect seem to have been characterized by a sequence of depositional stages involving varying

SARs and varying initial activity concentrations, spanning for a decade since middle 60's (the limit of the chronology). This corresponds with the early stage of urban development of the city after the independence of Algeria, and it may comprise the large flood of 1974.

The second transect comprises from middle 70's till ∼2006. Sedimentary conditions seem to have been relatively regular in this period, without distinguishable fingerprints neither from the earthquake of 1980 nor for the tsunami of 2003. The same is true for the 2001 flood in the Bab El Oued district of Algiers. Periáñez and Abril (2013) reported results from numerical simulations of the 2003 tsunami in Algiers. The maximum amplitude of the tsunami wave was close to 0.5 m along the bay shoreline, and below 0.2 m in the sampling site. The maximum water currents were of 0.25 m/s along the shoreline and below 0.1 m/s at the sampling site. Their associated shear stresses were of 0.16 Pa and 0.025 Pa, respectively; the last figure being below the threshold value

Table 5
Cluster analysis for the sediment core from Algiers Bay.

Parameter (from fit)		Sedimentary conditions	
Transect 1			
$-s_1$	0.0428 ± 0.0125	$A_{o,1}$	127 ± 6
b_1	4.8419 ± 0.0450	w_1	0.73 ± 0.21
Pearson r	-0.790	F_1	920 ± 270
m_1 discontinuity	6.61		
Transect 2			
$-s_2$	0.0784 ± 0.0052	$A_{o,2}$	94 ± 9
b_2	4.2649 ± 0.0365	w_2	0.385 ± 0.027
Pearson r	-0.988	F_2	360 ± 40
m_2 discontinuity	18.10		
Transect 3			
$-s_3$	0.033 ± 0.024	$A_{o,3}$	51 ± 15
b_3	2.731 ± 0.270	w_3	0.94 ± 0.69
Pearson r	-0.415	F_3	500 ± 400

In the Ln[$A(m)$] plot (Fig. 6), $A(m)$ is given in Bq·kg^{-1} and m in g·cm^{-2}. $A_{o,i}$ and w_i (i = 1,2,3 –it refers to transects or clusters) have units of Bq·kg^{-1} and g·cm^{-2}y^{-1}, respectively, and F_i are given in Bq·m^{-2}y^{-1}; s_i are slopes, and b_i the independent terms in the linear fit. Values and errors in $A_{o,i}$ for i > 1 have been estimated from Ln[$A(m')$] plots with a translation to the origin ($m' = m-m_1$ for i = 2; $m' = m-m_2$ for i = 3).

for resuspending clays, and the former being able to remobilize fine sand from the shoreline. These results are congruent with the absence of a distinguishable fingerprint of this tsunami in the studied sediment core.

The first transect comprises since ~2006 till the sampling time (2015). CIC-ages show moderate excursions out of the trend-line, revealing significant variability in the initial activity concentrations, but without a clear adscription to extreme events such as the 2014 earthquake. The variability seems then to be likely linked to anthropogenic impacts through the evolution of the urban planning. Recent SAR values (0.73 ± 0.21 g cm^{-2}y^{-1}) correspond to linear accretion velocities of 0.86 ± 0.25 cm/y (when accounting for early compaction – see Abril, 2003b).

3.7. Temporal records of pollutants

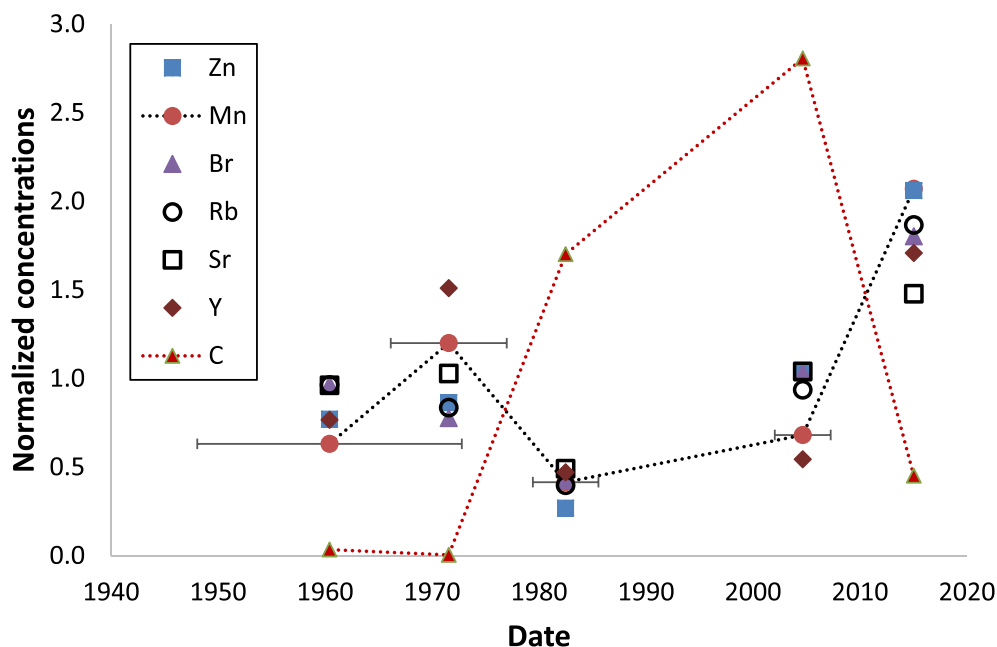Fig. 7 plots the normalized (to their arithmetic means) concentrations of some of the WDXRF-determined elements (Table 2) as a function of the date of their deposition onto the sediment. Although only five sediment slices were analyzed, results clearly show a common trend for Zn, Mn, Br, Rb, Sr and Y, with an absolute maximum at the most recent slice, and a minor relative peak at early 70's.

The enrichment factor (EF) provides an estimate of the anthropogenic influence on sediments, and it uses a normalization element (Loring and Rantala, 1992):

$$EF = \frac{C_a X_b}{C_b X_a}. \tag{8}$$

In Eq. (8) C_a and C_b are the examined metal content in the sample and background reference, respectively, and X_a and X_b are the content of the normalization element in the sample and the background reference, respectively. Values of EF < 2 indicates deficiency to minimal enrichment, the enrichment is moderate for values in the range 2–5, and severe for the range 5–20. The deepest sediment layer (42–44 cm) can be used as a reasonable estimate of the local reference background.

When using Al as normalization element, the group of analytes Mn, Zn, Br, Rb, Sr, Y and Pb show moderate enrichment only in the 0–1 cm surface layer (with minimum EF = 2.1 for Sr and maximum EF = 4.4 for Mn). This discards spurious enrichments merely due to an increase in the proportion of Al-silicates.

When using Fe as normalization element all the EF are below 2, indicating no enrichment, but for Mn in the 0–1 cm sediment slice, with EF = 2.1. Consequently the observed enrichments when using Al are co-occurring with Fe enrichment. Iron serves as a chemical tracer for Fe-rich clay minerals (Loring and Rantala, 1992). Thus, its increasing concentrations in recent times may be related to changes in the composition/provenance of the mass flows reaching the SWI and/or to anthropogenic pollution sources.

Although the composition of crystalline phases does not reveal significant changes over time (Table 3), these are evident for the amorphous phase. Thus, from Table 2, the percentage of Si has progressively decreased from 82.3% at the deepest sediment slice to 64.8% at the 0–1 cm depth interval (a relative decrease of 21%). The relative decrease in Al content is of 26% over the whole range of the chronology, while the Fe content increased by a 50%. But the major change is observed in the C content, which increases from 0.18% in the deepest layer to 14.1% in the 9–10 cm interval (Table 2 and Fig. 7). In terms of EF, for C it reaches

Fig. 7. Normalized (to their arithmetic means) concentrations of selected elements (from Table 2) as a function of the date of sediment deposition (chronology from Fig. 6). Dotted lines are only for guiding eyes. Horizontal bars are 1-σ uncertainty in ages.

values around 100 for Al and Fe normalizations. This cannot be explained by changes in the organic matter content (LOI in Table 1) nor by biogenic calcium-carbonates (the Ca content remains constant, Table 2). The origin of this enrichment of C in a lapse of time of three decades remains unexplained, but it could be linked to the activities of oil trade in the harbour, whose efficiency would have improved in recent times. The depth interval with high C content roughly matches the transect 2 in the ^{210}Pb-based geochronology (Fig. 6). Furthermore, the above scenario of a sediment composition varying over time (in terms of its content in major elements) is congruent with the also varying initial activity concentrations of ^{210}Pb$_{exc}$ inferred from the cluster analysis (Fig. 6 and Table 5).

The anthropogenic enhancement of fluxes of pollutants can be estimated from recent sedimentation rates and the excess concentration of each analyte (concentration found in the 0–1 cm layer minus the background level found in the 42–44 cm layer). In units of $g \cdot m^{-2} y^{-1}$ they take values of 152 for C, 58 for Fe, 1.22 for Mn, 0.26 for Zn, 0.21 for Sr, 0.10 for Rb, 0.08 for Br, and 0.07 for Pb (with a relative uncertainty of 30% contributed by SAR).

It is noted that diagenetic and geochemical processes are not considered. Indeed, they can sensibly influence the behaviour and the concentrations of the trace elements in the sediment as a function of the depth; and this is probably the reason why the Mn presents several EF as a function of the normalization element used.

4. Conclusions

The measured activity concentrations of ^{210}Pb, ^{226}Ra, ^{228}Ra, ^{228}Th and ^{40}K in the sediment core and the meaningful isotopic ratios were within typical values in the earth crust, and ^{137}Cs concentrations were relatively low. Consequently they do not pose any radioecological concern. Due to the low activity concentrations in reference organism estimated by the ERICA tool, and to the low consumption rates of local seafood from Algiers Bay, the committed effective dose integrated for 50 years for adults resulted of $3.2 \cdot 10^{-5}$Sv, far from producing any harmful effect.

The ^{210}Pb-based chronologies assuming a constant initial activity concentration and/or a constant rate of supply of ^{210}Pb$_{exc}$ (CIC, CRS and CF-CS models) failed to explain the high ^{137}Cs activity concentrations found at the deepest sediment layers.

Bulk density and normalized depth-distributions of LOI, ^{226}Ra, ^{212}Pb and ^{40}K revealed active early compaction and the absence of recognizable fingerprints of disruptions in the sedimentary sequence.

The relatively high inventories of ^{210}Pb$_{exc}$ and ^{137}Cs discarded pure water-column scavenging process as the only contribution to the fluxes of these radionuclides onto the SWI. Consequently fluxes must be also contributed by the radionuclide activities bound to the mass flows. This scenario makes unlikely non-ideal deposition effects, and it supports the application of the cluster analysis and the piecewise CF-CS and CIC models.

Results from the system time-averaging (STA) and water-column models for ^{137}Cs support the above view and provide a lower limit for the age of the deepest sediment slice (middle 60's), in reasonable agreement with the piecewise CF-CS chronology.

Despite the lack of ^{210}Pb and ^{137}Cs inventories, the modelling of ^{137}Cs in the water column, together with the application of piecewise ^{210}Pb dating model have allowed establishing a reliable chronology in this sediment core.

Fluxes of ^{210}Pb$_{exc}$ and sediment accumulation rates have both varied over the last five decades. Recent SAR values are of 0.73 ± 0.21 $g \cdot cm^{-2} y^{-1}$, which correspond to linear accretion velocities of 0.86 ± 0.25 cm/y.

The elemental analysis revealed noticeable changes over time in the contents of Si, Al and Fe. Moderate enrichments have been observed for Mn, Zn, Br, Rb, Sr, Y and Pb in the 0–1 cm sediment layer (when using Al as normalization element), being governed by Fe-rich carriers. The

major impact is observed in the carbon content, with EF of about 10^2 and covering a lapse of time of three decades since early 70's. Its origin remains unknown but it could be likely linked to oil trade operations in the Algiers harbour.

Declaration of competing interest

Acknowledgements

References

Abril, J.M., 2003a Difficulties in interpreting fast mixing in the radiometric dating of sediments using ^{210}Pb and ^{137}Cs. J. Paleolimnol. 30 (4), 407–414.

Abril, J.M., 2003b. A new theoretical treatment of compaction and the advective-diffusive processes in sediments. A reviewed basis for radiometric dating models. J. Paleolimnol. 30, 363–370.

Abril, J.M., 2004. Constraints on the use of Cs-137 as a time marker to support CRS and SIT chronologies. Environ. Pollut. 129, 31–37.

Abril, J.M., 2011. Could bulk density profiles provide information about recent sedimentation rates? J. Paleolimnol. 46, 173–186.

Abril, J.M., 2019. Radiometric dating of recent sediments: on the performance of ^{210}Pb-based CRS chronologies under varying rates of supply. Quat. Geochronol. 51, 1–14.

Abril, J.M., Brunskill, G.J., 2014. Evidence that excess ^{210}Pb flux varies with sediment accumulation rate and implications for dating recent sediments. J. Paleolimnol. 52, 121-13.

Abril, J.M., García-León, M., 1994. The integrated atmospheric flux effect in a radiogeochronological model. J. Environ. Radioact. 24, 65–79.

Abril, J.M., Gharbi, F., 2012. Radiometric dating of recent sediments: beyond the boundary conditions. J. Paleolimnol. 48, 449–460.

Abril, J.M., San Miguel, E.G., Ruiz-Cánovas, C., Casas-Ruiz, M., Bolívar, J.P., 2018. From floodplain to aquatic sediments: radiogeochronological fingerprints in a sediment core from the mining impacted Sancho Reservoir (SW Spain). Sci. Total Environ. 631–632, 866–878. https://doi.org/10.1016/j.scitotenv.2018.03.114.

Appleby, P.G., 1998. Dating recent sediments by ^{210}Pb: problems and solutions. In: Illus, E. (Ed.), Dating of Sediments and Determination of Sedimentation Rate. STUK A-145, Finland, pp. 7–24.

Aroua, N., Berezowska-Azzag, E., 2009. Contribution à l'étude de la vulnérabilité urbaine au risque d'inondation dans un contexte de changement climatique. Cas de la Vallée d'Oued El Harrach à Alger. Fifth Urban Research Symposium 2009: "Cities and Climate Change: Responding to an Urgent Agenda", Marseille, France.

Benamar, M.A., Toumert, I., Tobbeche, S., Tchantchane, A., Chalabi, A., 1999. Assessment of the state of pollution by heavy metals in the surficial sediments of Algiers Bay. Appl. Radiat. Isot. 50, 975–980.

Benfedda, A., Abbes, K., Bouziane, D., Bouhadad, Y., Slimani, A., Larbes, S., Haddouche, D., Bezzeghoud, M., 2017. The august 1st, 2014 (mw 5.3) moderate earthquake: evidence for an active thrust fault in the bay of Algiers (Algeria). Pure Appl. Geophys. 174, 1503–1511.

Boulahdid, M., Taieb Errahmani, D., Noureddine, A., Hocini, N., Ounadi, F., 2013. Les métaux traces dans les sédiments de la baie d'Alger. Rapp. Comm. int. Mer. M, dit. 40, 833p, 2013. http://www.ciesm.org/online/archives/abstracts/pdf/40/index.php#.

Brown, J.E., Alfonso, B., Avila, R., Beresford, N.A., Copplestone, D., Hosseini, A., 2016. A new version of the ERICA tool to facilitate impact assessment of radioactivity on wild plants and animals. J. Environ. Radioact. 153, 141–148.

Carroll, J., Lerche, I., 2003. Sedimentary Processes: Quantification Using Radionuclides. Elsevier, Oxford.

Chemrouk, O., Chabbi, N., 2016. Vulnerability of Algiers waterfront and the new urban development scheme. Procedia Eng. 161, 1417–1422.

Dadey, K.A., Janecek, T., Klaus, A., 1992. Dry-bulk density: its use and determination. In: Taylor, B., Fujioka, K., et al. (Eds.), Proceedings of the Ocean Drilling Program, Scientific Results, vol. 126, pp. 551–554.

Delfanti, R., Klein, B., Papucci, C., 2003. Distributions of ^{137}Cs and other radioactive tracers in the eastern Mediterranean: relationship to the deep water transient. J. Geophys. Res. 108 (C9), 8108. https://doi.org/10.1029/2002JC001371.

ICRP, 2012. Publication 119: compendium of dose coefficients based on ICRP publication 60. Ann. ICRP 41 (Suppl. 1), 1–130.

Klubi, E., Abril, J.M., Nyarko, E., Laissaoui, A., Benmansour, M., 2017. Radioecological assessment and radiometric dating of sediment cores from dynamic sedimentary systems of Pra and Volta estuaries (Ghana) along the equatorial Atlantic. J. Environ. Radioact. 178–179, 1–11.

Laissaoui, A., Benmansour, M., Ziad, N., Ibn Majah, M., Abril, J.M., Mulsow, S., 2008. Anthropogenic radionuclides in the water column and a sediment core from the Alboran Sea: application to radiometric dating and reconstruction of historical water column radionuclide concentration. J. Paleolimnol. 40, 823–833.

Larsson, C.M., 2008. An overview of the ERICA Integrated Approach to the assessment and management of environmental risks from ionising contaminants. J. Environ. Radioact. 99 (9), 1364e1370.

Lee, S.H., Mantoura, F.R., Povinec, P.P., Sanchez-Cabeza, J.A., Pontis, J.L., Mahjoub, A., Noureddine, A., Boulahdid, M., Chouba, L., Samaali, M., Reguigui, N., 2006. Distribution of anthropogenic radionuclides in the water column of the south-western Mediterranean Sea. Radioact. Environ. 8, 137–147.

Loring, D.H., Rantala, R.T.T., 1992. Manual for the geochemical analyses of marine sediments and suspended particulate matter. Earth Sci. Rev. 32, 235–283.

Luczak, C., Janquin, M.A., Kupka, A., 1997. Simple standard procedure for the routine determination of organic matter in marine sediment. Hydrobiologia 345, 87–94.

Mabit, L., Benmansour, M., Abril, J.M., Walling, D.E., Meusburger, K., Iurian, A.R., Bernard, C., Tarjan, S., Owens, P.N., Blake, W.H., Alewell, C., 2014. Fallout ^{210}Pb as a soil and sediment tracer in catchment sediment budget investigations: a review. Earth Sci. Rev. 138, 335–351.

McCall, P.L., Robbins, J.A., Matisoff, G., 1984. ^{127}Cs and ^{210}Pb transport and geochronologies in urbanized reservoirs with rapidly increasing sedimentation rates. Chem. Geol. 44, 33–65.

Machane, D., Bouhadad, Y., Cheikhlounis, G., Chatelain, J.L., Oubaiche, E.H., Abbes, K., Guillier, B., Bensalem, R., 2008. Examples of geomorphologic and geological hazards in Algeria. Nat. Hazards 45, 295–308. https://doi.org/10.1007/s11069-007-9167-5.

Naimi-Ait-Aoudia, M., Berezowska-Azzag, E., 2014. Algiers carrying capacity with respect to per capita domestic water use. Sustain. Cities Soc. 13, 1–11. https://doi.org/10.1016/j.scs.2014.03.006.

Noureddine, A., Menacer, M., Boudjenoun, R., Benkrid, M., Boulahdid, M., Kadi-hanifi, M., Lee, S.H., Povinec, P.P., 2006. ^{137}Cs in seawater and sediment along the Algerian coast. Radioact. Environ. 8, 156–164.

Noureddine, A., Benkrid, M., Maoui, R., Menacer, M., Boudjenoun, R., Kadi-hanifi, M., Lee, S.H., Povinec, P.P., 2008. J. Environ. Radioact. 99 (8), 1224–1232.

Periáñez, R., Abril, J.M., 2013. Modeling tsunami propagation in the Iberia–Africa plate boundary: historical events, regional exposure and the case-study of the former Gulf of Tartessos. J. Mar. Syst. 111, 223–234.

Robbins, J.A., 1978. Geochemical and Geophysical applications of radioactive lead isotopes. In: Nriago, J.P. (Ed.), Biochemistry of Lead in the Environment. Elsevier, Amsterdam, pp. 285–393.

Robbins, J.A., Edgington, D.N., 1975. Determination of recent sedimentation rates in Lake Michigan using ^{210}Pb and ^{137}Cs. Geochem. Cosmochim. Acta 39, 285–304.

Robbins, J.A., Holmes, C., Halley, R., Bothner, M., Shinn, E., Graney, J., Keeler, G., ten Brink, M., Orlandini, K.A., Rudnick, D., 2000. Time-averaged fluxes of lead and fallout radionuclides to sediments in Florida Bay. J. Geophys. Res. 105, 28805–28821.

Sánchez, C.I., García-Tenorio, R., García-León, M., Abril, J.M., El-Daoushy, F., 1992. The use of ^{137}Cs in marine and lacustrine sediment dating. Nucl. Geophys. 6 (3), 395–403.

Sánchez-Cabeza, J.A., Ruíz-Fernández, A.C., 2012. ^{210}Pb sediment radiochronology: an integrated formulation and classification of dating models. Geochem. Cosmochim. Acta 82, 183–200.

UNEP/WHO, 1999. Identification of Priority Pollution Hot Spots and Sensitive Areas in the Mediterranean. MAP Technical Reports Series No.124. UNEP, Athens.

UNSCEAR, 2008. Sources and Effects of Ionizing Radiations, vol. 1. United Nations Publications, New York.

Vecchio, A., Anzidei, M., Carbone, V., 2014. New insights on the tsunami recording of the May, 21, 2003, Mw 6.9Boumerdès earthquake from tidal data analysis. J. Geodyn. 79, 39–49.

Vidmar, T., 2005. Efftran - a Monte Carlo efficiency transfer code for gamma-ray spectrometry. Nucl. Instrum. Methods Phys. Res. A 550, 603–608.

Wright, S.M., 2016. Predicted Caesium-137 Deposition from Atmospheric Nuclear Weapons Tests. NERC Environnemental Information Data Centre. https://doi.org/10.5285/c3e530bf-af20-43fc-8b4b-92682233ff08.